Journal of Marine Science and Application (2019) 18:271–281
https://doi.org/10.1007/s11804-019-00096-4

RESEARCH ARTICLE

Application of a RaNS and PF-Based Method to Study the Resistance and Motion of a Bulk Carrier

Hafizul Islam[1] · Mashiur Rahaman[2] · M. Rafiqul Islam[2] · Hiromichi Akimoto[3]

Received: 5 January 2018 / Accepted: 27 September 2018 / Published online: 18 July 2019

Abstract

Resistance prediction of ships using computational fluid dynamics has gained popularity over the years because of its high accuracy and low cost. This paper conducts numerical estimations of the ship resistance and motion of a Japan bulk carrier model using SHIP_Motion, a Reynolds-averaged Navier–Stokes (RaNS)-based solver, and HydroSTAR, a commercial potential flow (PF)-based solver. The RaNS solver uses an overset-structured mesh and discretizes the flow field using the finite volume method, while the PF-based solver applies the three-dimensional panel method. In the calm water test, the total drag coefficient, sinkage, and trim were predicted using the RaNS solver following mesh dependency analysis, and the results were compared with the available experimental data. Next, calm water resistance was investigated for a range of Froude numbers. The added resistance in short-wave cases was simulated using both RaNS and PF solvers, and the results were compared. The PF solver showed better agreement with the RaNS solver for predicting motion responses than for predicting added resistance. While the added resistance results could not be directly validated because of the absence of experimental data, considering the previous accuracy of the RaNS solver in added resistance prediction and general added resistance profile of similar hull forms (bulk carriers), the prediction results could be concluded to be reliable.

Keywords Computational ship hydrodynamics · Japan bulk carrier · RaNS simulation · Potential flow simulation · Total drag resistance · Added resistance

Article Highlights
- Calm water simulations are performed for a JBC model at different Froude numbers using a RaNS solver, after verification and validation study
- Added resistance simulations are performed using both a RaNS- and PF-based solver
- The results provide initial reference data for future studies of the JBC model

✉ Mashiur Rahaman
mashiurrahaman@name.buet.ac.bd

[1] CENTEC, Instituto Superior Tecnico, University of Lisbon, 1049-001 Lisbon, Portugal

[2] Department of Naval Architecture and Marine Engineering, Bangladesh University of Engineering and Technology, 1000, Dhaka, Bangladesh

[3] Center for the Advancement of Research and Education Exchange Network in Asia (CAREN), Graduate School of Engineering, Osaka University, Osaka 565-0871, Japan

1 Introduction

Present-day challenges in the shipping and shipbuilding industry include minimization of energy consumption, assurance of maximum protection for the marine environment, and maximization of the efficiency and economy of maritime operations while preserving safety and comfort. Ship designers give importance to performance predictions to maintain their competitive edge over other companies. Ship officers desire fast and safe ships with good and reliable performance in actual sea conditions, ship owners consider maximum profit when selecting operating conditions, and passengers, in general, search for inexpensive transportation while maintaining environmental standards. Thus, ship design has become increasingly complex, and this growing complexity of modern ships has made the use of computational fluid dynamics (CFD) in the design and evaluation phase an increasingly attractive endeavor. CFD and other potential flow (PF)-based solvers offer a low cost and relatively easy alternative to

traditional design evaluation methods and facilitates better and more efficient vessel designs.

Seakeeping and maneuverability predictions in the design phase are not new to the shipping industry. According to reports presented at the 20th–24th IITC and Gothenburg conference proceedings, after decades of development in the 1970s and 1980s, a full Reynolds stress turbulence model was first introduced in the Tokyo 1994 workshop with impressive results. To further facilitate CFD developments, three new ship models, namely, KRISO Container Ship (KCS), KRISO Very Large Crude Carrier (KVLCC), and David Taylor Model Basin (DTMB) 5415, were introduced with experimental results for validation at the Gothenburg 2000 workshop (Larsson et al. 2003). Self-propulsion systems including CFD models were also presented in this workshop. The Gothenburg 2010 workshop (Larsson et al. 2011) discussed global and local flow variables, grid-dependency, and turbulence modeling. The Tokyo 2015 workshop provided ship resistance data with and without a rudder and propeller.

Soon after reports of successful flow field simulation and calm water resistance prediction were published, attention focused on added resistance prediction. Many computational results for ship motions using Reynolds-averaged Navier–Stokes (RaNS) methods have been produced in the last few years. Orihara and Miyata (2003) used a code called Wisdam-*X* that solved an overlapping grid system using the finite volume method (FVM) to solve ship motions in regular head waves and evaluated the added resistance of a series of different bow-forms for a medium-speed tanker. Deng et al. (2010), Moctar et al. (2010), and Sadat-Hosseini et al. (2010) presented added resistance prediction results for KVLCC2 in head waves in the Gothenburg 2010 workshop for wavelength ratios of 0.6, 1.1, and 1.6. Deng et al. (2010) simulated cases using the ISISCFD RaNS solver, Moctar et al. (2010) used open FOAM and Comet RaNS codes, and Sadat-Hosseini et al. (2010) used CFDShip-Iowa. Kim et al. (2013) validated added resistance cases for KVLCC2 using a RaNS code called WAVIS, which was developed by KRISO. A detailed study of both steady and unsteady ship motions was also conducted by Simonsen et al. (2013), who compared experimental results for KCS with CFD predictions gained using CFDShip-Iowa and the commercial code Star-CCM+. Islam and Akimoto (2015) and Islam et al. (2017) used an in-house code SHIP_Motion and a commercial PF code to perform calm water and added resistance simulation of the KVLCC2 model. Kim et al. (2017) also performed a comparative study for the KVLCC2 model using Star-CCM+ and a PF solver. Shen et al. (2015) modified the open source CFD solver, OpenFOAM, to incorporate overset grid and performed maneuvering simulation for the appended hull. Sigmund and el Moctar (2018) used COMET and modified OpenFOAM solver to perform added resistance simulations for four different hull types.

Parallel to the development of different RaNS solvers, PF-based solvers have also been investigated by several researchers. Since PF solvers cannot realize viscous effects, they are not generally used for predicting calm water resistance. Thus, PF-based solvers are mostly applied to added resistance prediction.

Maruo (1957) was the first to develop a formula to calculate added resistance based on the conservation principle of energy and momentum. Later, Gerritsma and Beukelman (1972) proposed the radiated energy method, where ship motion was derived from strip theory. Fuji and Takahashi (1975) expanded Maruo's formula by considering added resistance in short waves. Faltinsen et al. (1980) developed a direct pressure integration method that calculated the added resistance by pressure integration over the instantaneous position of the wetted surface. Journee (2001) applied a linear strip theory–based solver together with Gerritsma and Beukelman's radiated energy method and showed that added resistance is under-predicted for short waves as the three-dimensional (3D) bow wave diffraction is dominant but not taken into account by strip theory. Kashiwagi (2009) modified Maruo's approach using enhanced unified theory and produced a method that is capable of considering 3D and forward speed effects, both of which are usually ignored in strip theory; this method, however, shows limitations when considering short-wave conditions. Kim and Kim (2011) adopted the Rankine panel method in the time domain for numerical calculations of added resistance. The results of this work revealed that the application of different linearization schemes produces different accuracy results for different conditions; however, overall, the results were satisfying and in good agreement with experimental data. The Rankine panel method was re-validated by Seo et al. (2014) for both container and tanker ship. Söding et al. (2014) also performed the Rankine panel method–based simulations for a Wigley hull, a tanker, and a container vessel.

Although CFD and numerical methods have been used in hydrodynamic studies for several decades now, confidence in their results remains low. Most of the available publications on RaNS and PF methods are based on verification and validation studies, and new findings gained using CFD results are doubted without confirmation by experimental results. However, experimental studies are also not devoid of uncertainties. Today, numerical simulations are mature enough to provide qualitative, if not quantitative, assessments of ship hydrodynamics. This paper attempts to provide a qualitative assessment of the resistance and motion of the Japan bulk carrier (JBC) in both calm waters and waves using CFD. The ship model was introduced in the Tokyo 2015 workshop, but very limited experimental data for this model are available. The results of this work could serve as an initial reference for other studies on the model.

2 Computational Method

2.1 Mathematical Model of the RaNS Solver

The mathematical model of the RaNS solver used, SHIP_Motion, has been elaborately discussed by Kim et al. (2015), Orihara (2005), and Akimoto and Miyata (2002) in their respective works. Thus, only a brief overview of the solver is provided in this paper.

Governing equations are the three-dimensional, time-dependent, incompressible RaNS equation, and the continuity equation for fluid velocity and pressure. Two sets of the Cartesian coordinate systems, body-fixed and earth-fixed, are used. Spatial discretization is conducted via the FVM. Third-order upwind differencing is used for advection, while discretization in space is conducted via the second-order central difference scheme. Physical values are defined in a staggered manner, that is, the pressure is defined at the cell or volume center and the velocity quantities are defined at face centers.

Free surface capturing is accomplished via the marker density method, in which the third-order upwind scheme performs space differentiation and the second-order explicit Adams–Bashforth method achieves time differentiation. The kinematic condition in free surface for mass conservation is treated using the density-function method. Two types of turbulence models are incorporated, namely, the zero-equation Baldwin–Lomax model and the dynamic sub-grid scale model. Although the zero-equation turbulence model cannot generate a detailed turbulent flow field, it is sufficient to capture the exchange of energy due to turbulence stress. The lower-order model significantly reduces resource requirements during the simulation. The wall function is used to reduce mesh dependency during the capture of boundary layer properties. Thus, a non-dimensional wall distance ($y+$) value higher than 1 could be applied. In the presented simulations, the highest mesh resolution contains a $y+$ value less than 1 only for the first cell near the hull surface; the cell size gradually increases from the next layer of cells.

A marker and cell-type pressure solution algorithm is employed. The pressure is obtained by solving the Poisson equations using the successive overrelaxation method, and velocity components are gained by correcting the velocity predictor with the implicitly evaluated pressure. In the overlapping grid system, the inner domain moves according to the floating body's equation of motion, while the outer domain represents a free surface. Grid points located at the overlapping region exchange information through interpolation to update both domains at every time step. Parallel processing in the solver is conducted by the shared memory model of OpenMP.

In this research, an overset-structured single-block mesh system is used. A coarse rectangular outer mesh with high resolution around the free surface is used to capture the free surface deformation, and the fine O–H type inner mesh around the hull surface is used to capture the flow properties around the hull surface. For both domains, the orientation of the X-axis is from bow to stern, the Y-axis is positive toward the starboard, and the Z-axis is upward-positive. Figure 1 shows the fine inner mesh (a), the coarse outer mesh (b), and their combined arrangement (c).

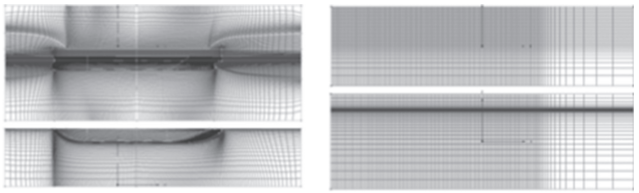

(a) Inner mesh domain (front and bottom views)

(b) Outer mesh domain (top and front views)

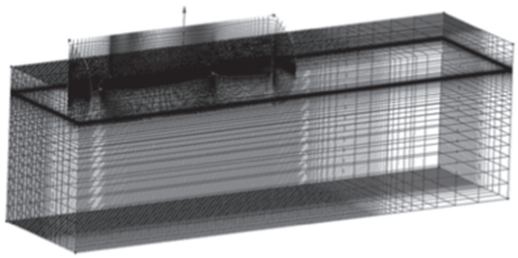

(c) Combined mesh domains (isometric view)

Fig. 1 Mesh arrangement used for the simulations

2.2 Mathematical Model of the Potential Flow–Based Solver

The PF-based solver used here, HydroSTAR, is a commercial solver developed by BUREAU VERITAS, France. The solver has been under development since 1991 and provides a complete solution of first-order low-frequency wave loads for floating bodies with or without forward speed in deep water and in finite water depths. The theoretical detail of the code has been elaborately explained by Chen (2004) and Chen and

Table 1 Specifications of the bulk carrier ship model, JBC

Specification		JBC ship (full scale)
Length between perpendicular	L_{pp} (m)	280.0
Breadth	B (m)	45.0
Depth	D (m)	25.0
Draft	T (m)	16.5
Wetted surface area	S (m^2)	19 556.1
Displacement volume	V (m^3)	178 369.9
LCB from mid-ship (fwd+)	L_{CB} (m)	7.133
K_{yy}	K_{yy} (m)	0.25 L_{pp}

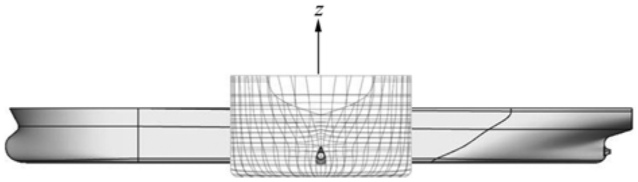

Fig. 2 Side view and body planes of the JBC model

Rezende (2009). A brief overview of the solver is provided below, following Chen's papers.

HydroSTAR follows an earth- and body-fixed, i.e., sign rule, i.e., the Z-axis is upward-positive and X is positive in the direction of flow propagation. The solver follows the Laplace equation, $\varphi_{yy}^R + \varphi_{zz}^R = 0$, i.e., fluid is inviscid and irrotational, and the radiation potential in the $Y$and Z direction is zero. The linear free surface boundary condition is given by $-\omega^2\varphi_j^R + g\frac{\delta}{\delta z}\varphi_j^R = 0$, when $Z = 0$. The bottom boundary condition, $\nabla\varphi^R \to 0$, when $Z \to -\infty$, and the radiation condition at infinity, $\frac{\delta\varphi^R}{\delta r} - i\frac{\omega^2}{g}\varphi^R = 0$, when $|r| \to \infty$. The time-dependent fluid motion is considered to be simple harmonic, and the velocity potential is given by:

$$\Phi = Re\left[\varphi(x,y,z)\mathrm{e}^{-\mathrm{i}\omega t}\right] \tag{1}$$

$$\varphi = -i\omega\left[(\varphi_\mathrm{o} + \varphi_7)\zeta_a + \left(X_j\varphi_j\right)\right] \tag{2}$$

$$\varphi_o = \frac{-ig\zeta_a}{\omega}\frac{\cosh[k(z+h)]}{\cosh kh}\mathrm{e}^{ik(x\cos\alpha + y\sin\alpha)} \tag{3}$$

In the above equations, φ is the potential; its subscript defines the direction and its superscript defines the type of potential. In addition, ω is the frequency of incoming incident waves, g is a gravitational constant, φ_o is the incident wave potential, φ_7 is the diffraction wave potential, ζ_a is the incident wave amplitude, and α is the wave heading angle.

The integral equation of the first-order problem is derived by using the Green function:

$$\varphi_j(x,y,z) = \frac{1}{4\pi}\iint \sigma_j(\xi,\eta,\zeta)G(x,y,z;\xi,\eta,\zeta)\mathrm{d}s \tag{4}$$

where (ξ, η, ζ) refers to a point on surface S and $\sigma_j(\xi, \eta, \zeta)$ represents an unknown source distribution. The finite-depth Green function is decomposed into the deep-water Green function and two regular functions representing the influence of the seabed. The regular functions are evaluated accurately and approximated by Chebyshev polynomials of three variables.

To construct the solver, in the momentum equation, a fictitious force depending on the fluid velocity is introduced to represent the energy dissipation of various sources without modifying the inviscid and irrotational properties. Thus, a damping term with the same parameter is present in the classical boundary condition over the free surface. By applying the perturbation procedure, the boundary value problems of the first and second order are then developed.

The first-order wave exciting forces and oscillatory forces created by the dynamic pressure acting on the rigid body is obtained by:

$$F_k\mathrm{e}^{-\mathrm{i}\omega t} = -i\rho\omega\mathrm{e}^{-\mathrm{i}\omega t}\int\{\varphi_{\mathrm{o}+}\varphi_7\}n_k\mathrm{d}s \tag{5}$$

$$F_{kj} = -\rho\omega^2\mathrm{e}^{-\mathrm{i}\omega t}\sum_{j=1}^{6}\iint\varphi_i n_k\mathrm{d}s \tag{6}$$

where F_k represents the k-th component of wave exciting forces and F_{kj} represents the k-th component of force caused by the motion in the j-th direction. Here, like j, k also represents the degree of freedom of motion. The added mass and damping coefficients are respectively represented by:

$$a_{kj} = -\rho.\mathrm{Re}[\iint\varphi_j n_k\mathrm{d}s] \tag{7}$$

$$b_{kj} = -\rho\omega.\mathrm{Im}[\iint\varphi_j n_k\mathrm{d}s] \tag{8}$$

Finally, the equation of motion in the frequency domain is represented by:

$$\sum_{j=1}^{6}\left(M_{kj} + a_{kj}\right)\hat{\ddot{X}}_j + b_{kj}\dot{X}_j + CX_j = F_k; k = 1,2,3,\ldots,6; j = 1,2,3,\ldots,6 \tag{9}$$

where $\boldsymbol{M}_{kj}$ is the inertia matrix in the k direction due to j motion, c is the hydrostatic restoring force coefficient matrix, $\boldsymbol{X}_j$ is the vector containing three translational and rotational oscillations about the coordinate axes in the j direction, and F_k is the wave exciting force in the k direction.

To deal with irregular frequencies, a mathematical model is used. First, the locations of irregular frequencies are determined by eigenfrequencies, after which these frequencies are eliminated using the extended integral equation method.

Table 2 Mesh configurations used in the calm water simulations

Mesh	Dimension of the inner domain			Dimension of the outer domain			Total mesh
	I	J	K	I	J	K	
Mesh 1	198	27	111	192	45	63	1 137 726
Mesh 2	142	20	78	192	45	63	765 840
Mesh 3	107	15	55	192	45	63	632 595

Table 3 Grid-dependency analysis for calm water simulations based on the GCI method

Item		Total drag coefficient C_t (e-3)	Sinkage (m)	Trim (°)
Fr number		0.1420	0.1420	0.1420
Output values	$\emptyset_1$ (mesh 1)	4.3400	− 0.0930	− 0.1200
	$\emptyset_2$ (mesh 2)	4.1200	− 0.1100	− 0.1440
	$\emptyset_3$ (mesh 3)	4.3100	− 0.1150	− 0.1500
Refinement ratio	$r_{21} = h_2/h_1$	1.3900	1.3900	1.3900
	$r_{32} = h_3/h_2$	1.3600	1.3600	1.3600
Difference of estimation	$\epsilon_{21} = \emptyset_2 - \emptyset_1$	− 0.2200	− 0.0170	− 0.0240
	$\epsilon_{32} = \emptyset_3 - \emptyset_2$	0.1900	− 0.0050	− 0.0060
Convergence	$\epsilon_{32}/\epsilon_{21}$	− 0.8636	0.2941	0.2500
Order of accuracy	p	0.4300	3.3800	3.8500
Extrapolated values	${\emptyset^{21}}_{\text{ext}}$	5.7863	− 0.0847	− 0.1106
	${\emptyset^{32}}_{\text{ext}}$	2.7759	− 0.1073	− 0.1414
Approximate relative error	${e^{21}}_{\text{a}}$	− 0.0507	0.1828	0.2000
	${e^{32}}_{\text{a}}$	0.0461	0.0455	0.0417
Extrapolated relative error	${e^{21}}_{\text{ext}}$	− 0.2499	0.0982	0.0850
	${e^{32}}_{\text{ext}}$	0.4842	0.0255	0.0187
Grid convergence index (GCI)	${\text{GCI}^{21}}_{\text{fine}}$	− 0.4165	0.1118	0.0979
	${\text{GCI}^{32}}_{\text{mid}}$	0.4078	0.0311	0.0230

2.3 Ship Model

The ship model simulated in this research is the JBC, a capesize bulk carrier jointly introduced by the National Maritime Research Institute (NMRI), Yokohama National University, and the Shipbuilding Research Centre of Japan for the Tokyo 2015 workshop (2015). Table 1 provides details of the JBC model, and Fig. 2 shows its side view and body plan.

2.4 Computational Resource

The use of the OpenMP memory-sharing model in the RaNS solver limits its applicability to multi-cores of only one node, not a cluster of nodes. Each simulation in this paper was performed in a single node composed of an Intel(R) Corei7 CPU with eight cores, clock speed of 2.27 GHz, and 8 GB of physical memory. The standard non-dimensional time step used was 1.5×10^{-4}, and, to simulate each non-dimensional time for added resistance, the required physical time was about 80 min per case. All simulations were run up to eight non-dimensional times to achieve stable oscillatory motion.

For the PF-based code, a computer with the same configuration described above was used. However, the time required to run the frequency domain–based simulation was much smaller than that required by the RaNS solver. The PF solver took roughly 10 min to run each frequency step, with the total simulation time being roughly 6 h.

3 Results

3.1 Calm Water Resistance Prediction by RaNS Solver

Calm water resistance prediction involves estimation of the drag force of a ship moving forward in calm water. The ship resistance is the sum of the frictional resistance and pressure

Table 4 Calm water simulation results for three different configurations

	Total drag resistance ($\times 10^{-3}$)			Sinkage (% L_{pp})			Trim (°)		
Mesh	CFD	EFD	Deviation (%)	CFD	EFD	Deviation (%)	CFD	EFD	Deviation (%)
Mesh 1	4.34	4.29	1.16	− 0.093	− 0.086	− 8.14	− 0.12	− 0.180	33.33
Mesh 2	4.12	4.29	3.96	− 0.11	− 0.086	− 27.9	− 0.144	− 0.180	20
Mesh 3	4.31	4.29	− 0.466	− 0.115	− 0.086	− 33.7	− 0.15	− 0.180	16.67

Table 5 Calm water simulation results of the JBC model at different Froude and Reynolds numbers

Froude number, *Fr*	Reynolds Number, *Rn* ($\times 10^6$)	Total drag resistance, C_t ($\times 10^{-3}$)	Sinkage (% L_{pp})	Trim (°)
0.1010	5.31	4.64	− 0.047	− 0.057
0.1194	6.27	4.44	− 0.066	− 0.081
0.1377	7.23	4.42	− 0.091	− 0.113
0.1423	7.46	4.34	− 0.093	− 0.120
0.1469	7.72	4.27	− 0.103	− 0.130
0.1515	7.96	4.27	− 0.111	− 0.140

resistance. Frictional resistance arises from the hull surface friction, and pressure resistance comes from the resistance produced by waves and the viscous pressure resistance encountered by the ship during forward motion.

For grid-dependency analysis in calm water resistance prediction, three mesh resolutions for the inner mesh are tested. The mesh resolutions applied are shown in Table 2. For proper result prediction, viscous and pressure force near the hull surface are captured. Thus, mesh distribution was performed to provide a high resolution near the hull surface area and gradually enlarge the cell size near the domain boundaries.

Grid uncertainty analysis was performed following the procedure proposed by Celik et al. (2008). The results are reported in Table 3. During uncertainty analysis, the grid resolution in the *X*, *Y*, and *Z* direction, i.e., the entire inner domain, was considered. According to the findings, whereas the resistance prediction shows oscillatory convergence, both sinkage and trim show monotonous convergence. Thus, both sinkage and trim show low levels of uncertainty with low values of grid convergence index (GCI). By contrast, the GCI for resistance prediction is relatively high, likely because refinement was limited to the inner domain and not performed in the outer domain as well. Furthermore, the coarse mesh resolution may have been too low, causing poor solution of the flow field and over-estimation of the pressure. Nevertheless, this study does not show divergence, which indicates that monotonous convergence may be achieved by excluding the last coarse mesh and using a high mesh resolution as the fine mesh.

Next, for validation, the results of calm water simulation for the JBC model were compared with experimental data, as shown in Table 4. The experimental data were taken from the NMRI and presented in the Tokyo 2015 workshop (2015).

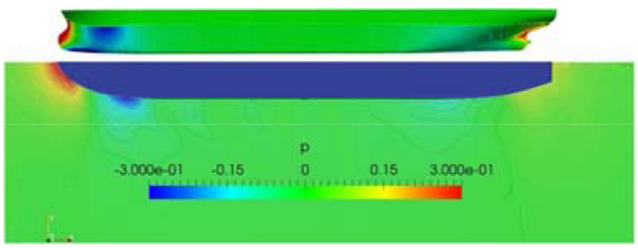

Fig. 3 Pressure distribution on the JBC hull surface and on the free water surface during calm water motion at a Froude number 0.142

According to the results, mesh 1, which features the highest resolution among the meshes applied, predicted the total resistance with good accuracy. The sinkage predictions are also accurate, and, although the deviation found is approximately 8%, the actual difference is only a few millimeters, which is practically insignificant. Unfortunately, the trim results show relatively poor agreement with the experimental data; however, improvements are obtained with decreasing mesh resolution. This exception in validation is likely due to the assumption of the CFD solver that the vertical center of gravity (KG) is at draft level (0.0 m); in the experiment, KG is actually − 0.011 m. Although the difference in KG is small, it clearly influences the trim results. While the assumption of the solver was incorrect, considering the time and resources required for re-running the simulation cases, it was avoided. Besides, the difference in KG position is too small to influence other results.

While the total resistance prediction results for mesh 3 show better predictions compared with those for mesh 1, this finding is probably caused by over-estimation of the pressure force near the hull due to excessively large mesh spacings. Overset meshing also complicates the exchange of information in the overset region if the mesh spacing in the inner grid is larger than the spacing in the outer grid. Considering the uncertainty level predicted from the uncertainty study and the deviation of simulation results from the experimental ones, both total drag prediction and sinkage results are validated. However, the trim results could not be validated since the predicted uncertainty (GCI) is lower than the deviation of the result.

After validation, the fine mesh resolution (mesh 1) and the same simulation settings were used with varying Froude and Reynolds numbers to predict the ship resistance and motion at different operational conditions. The results are shown in Table 5.

In case of ship motion through calm water, maximum resistance is observed at the bow and stern of the ship. This scenario is demonstrated by Fig. 3, which shows the pressure distribution on the ship hull and free water surface. Since the blunt bow propels through the water ahead, a negative pressure region is created just behind the bow front. Relatively high pressures are also observed in the stern section due to the partly submerged transom stern and vortex separation.

Table 6 Conditions and mesh configurations for simulation of the JBC in head waves

Specification	JBC
Froude number	0.142
Reynolds number	7.46×10^6
Wave amplitude, A/L	0.005
Degrees of freedom	2DOF (heave and pitch)
Number of grid points ($n_i \times n_j \times n_k$) inner/outer	$198 \times 27 \times 111/192 \times 45 \times 63$
Computational domain size inner (half domain)/outer (half domain)	$1.8\ L_{pp} \times 0.35\ L_{pp}$ (R)/$3.8\ L_{pp} \times 1\ L_{pp} \times 1\ L_{pp}$
Minimum grid spacing in longitudinal direction (inner/outer)	0.0012/0.0187
Minimum grid spacing in radial/lateral direction (inner/outer)	0.0008/0.0198
Minimum grid spacing in girth-wise/vertical direction (inner/outer)	0.0008/0.00068

3.2 Added Resistance Prediction by RaNS Solver

Added resistance mainly originates from the forces encountered by a ship as it makes its way through waves. This resistance component is created by the loss of energy to the radiated waves caused by ship motion and the diffraction of incident waves on the ship hull. However, the energy distribution between these two components depends on the ratio of incident wavelength to ship length (λ/L). For wavelengths up to half the ship length, the main contributor to resistance is the reflection of incident waves at the bow. In case the wavelength is around L, the ship motion accounts for the principal resistance. The resonance point for wave-induced ship motion also occurs within this wavelength. Long waves, i.e., $\lambda/L > 2.0$, result in minor ship motion; thus, the added resistance is low and approaches zero with increasing wavelength. The second-order effects of the wave–body interaction create an average drift force that manifests as resistance during the ship's forward motion. During added resistance calculations, sufficient mesh resolutions are required at the bow and stern to properly capture radiated waves and at the entire hull form near the water line to capture incident waves. Employing the appropriate resolution and dimension of the outer mesh is also important to capture the wave elevation and spread with reasonable accuracy.

For this paper, only short-wavelength cases were predicted, since large ships, such as the JBC, are rarely exposed to wavelengths beyond 0.8 L in their regular voyage routes, (Fuji and Takahashi 1975; Kim et al. 2013). Thus, the wavelengths covered in this paper should be sufficient to predict the ship's encountered resistance in case of the regular voyage. Since no experimental data for added resistance for the JBC are available at the moment, a direct validation study was not possible. However, the solver, SHIP_Motion, has previously been validated by several researchers for added resistance prediction in different hull models (Islam 2015; Orihara 2005; Ock 2014). Islam and Akimoto (2015) validated the solver for added resistance predictions for KVLCC2, which features a hull form very similar to that of the JBC. To ensure reliability, the same mesh resolution and distribution processes used by Islam and Akimoto (2015) for KVLCC2 simulation were applied to the JBC. Thus, the predicted results for the JBC can be assumed to be within reasonable accuracy.

All simulations were performed in symmetric conditions, i.e., half of the hull (port side hull) was simulated and only heave and pitch motion were set free (two degrees of freedom). The hull form contained an extended deck in the inner mesh to avoid the Green water problem. To convert simulation results to non-dimensional values, the following conversions were used.

Table 7 Head wave simulation results for the JBC model using SHIP_Motion

Wave Length, λ/L	Wave amplitude, A/L	Added resistance coefficient	Heave RAO	Pitch RAO
0.3	0.005	1.90	0.004	0.001
0.4	0.005	2.47	0.012	0.001
0.5	0.005	2.81	0.010	0.013
0.6	0.005	2.87	0.046	0.021
0.7	0.005	2.87	0.062	0.002
0.9	0.005	3.75	0.080	0.160
1.1	0.005	7.46	0.800	0.654
2	0.005	1.84	0.480	1.132

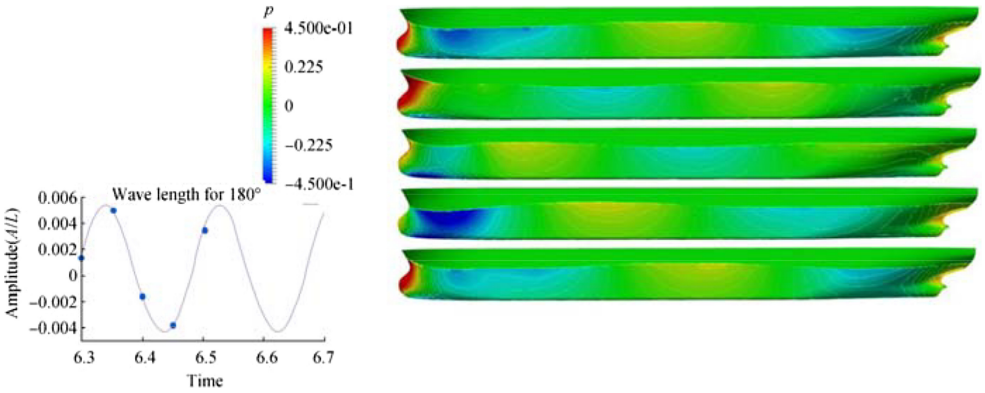

Fig. 4 Pressure distribution (unit scale) on the hull surface of the JBC at a wavelength of 0.6 L_{pp} and amplitude of 0.005 L_{pp} in head waves

Added resistance coefficient:

$$C_{aw} = Fr^2 \times \frac{1}{(A/L_{pp})^2} \times \left(\frac{L_{pp}}{B}\right)^2 \times \Delta f \tag{10}$$

where Fr is the Froude number, B is the ship's width, and Δf is the difference between the non-dimensional wave drag force and the calm water drag force.

Heave response amplitude operator (RAO):

$$\frac{Z}{A} = \frac{Z/L_{pp}}{A/L_{pp}} \tag{11}$$

where z is the heave amplitude, L_{pp} is the ship length between perpendiculars, and A is the incoming wave amplitude.

Pitch RAO:

$$\frac{\theta}{Ak} = \frac{\theta \times \lambda / L_{pp}}{(A/L_{pp}) \times 360} \tag{12}$$

where θ is the pitch amplitude, L_{pp} is the ship length between perpendiculars, A is the incoming wave amplitude, and λ is the wavelength.

The mesh configuration and simulation conditions for head wave cases for the JBC are described in Table 6, and the added resistance simulation results are shown in Table 7.

As can be seen in Table 7, the added resistance is directly related to the motion of the ship. As the heave and pitch motions increase, the added resistance also increases. As the wavelength approaches the ship length, the ship motion increases rapidly and the added resistance increases. Thus, when selecting voyage routes for such ships, seas with low wavelengths are preferred.

To further illustrate the results, pressure distributions on the hull surface during encounters with waves of length 0.6 L_{pp} and amplitude 0.005 L_{pp} are shown in Fig. 4. The figure also shows wave profiles on the bow front at each step shown. The ship's blunt bow front encounters maximum pressure when encountering head waves. The submerged transom stern also encounters relatively high pressure, followed by flow separation, which is difficult to simulate in the PF method. Thus, high turbulence is observed after the stern section.

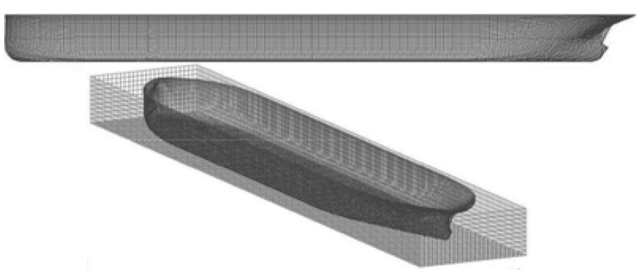

Fig. 5 Panel-generated hull surface of the JBC

3.3 Added Resistance Prediction of the PF-Based Solver

In PF solvers, added resistance is predicted by calculating the wave diffraction and radiation caused by ship motion. Since PF solvers simulate non-viscous flow, turbulence is completely ignored, and predictions are made on the basis of linear flow theory. The simulations are also performed mostly in the frequency domain.

For the running simulation in HydroSTAR, a 3D panel mesh was generated around the hull geometry using HydroSTAR mesh generation tool, HSMSH. The tool uses the body plan of the ship and information about the types of the fore and aft parts of the ship to generate a panel mesh. HydroSTAR reads the hull form using X, Y, and Z coordinates. The hull form is divided into several sections in the longitudinal direction, and then each longitudinal section is divided into several vertical or radial sections. In the dataset, each longitudinal section is represented by its X coordinate and the radial sections are represented by Y and Z coordinates. After HydroSTAR reads the hull form, HSMSH generates the panel mesh following the defined number of panels.

The number of panels used for the presented simulation cases was 300 × 50, i.e., 300 sections in the longitudinal direction and 50 sections in the radial direction. According to Pelaez et al. (2000), to achieve a panel size–independent

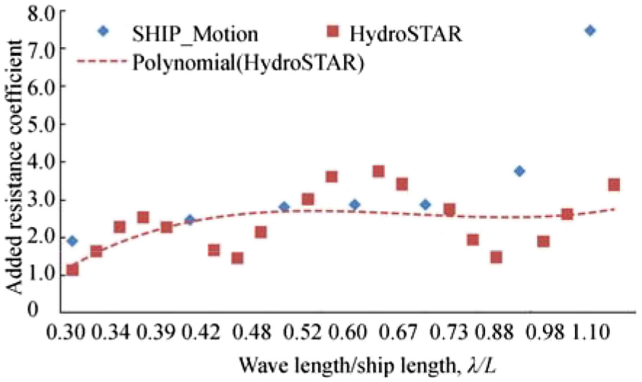

Fig. 6 Added resistance coefficients predicted for the JBC using SHIP_Motion and HydroSTAR

solution, the panel size in the wave propagation direction should be less than 20% of the shortest wavelength used in the simulations. Furthermore, according to DNV, the diagonal length of individual panels should be 1/6th of the shortest wavelength for proper convergence. The number of panels used for the simulations is well within the stated limits. Figure 5 shows the hull surface with panels. Although the figure also shows control of the surface for second-order drift load calculations, the calculation results of this load are not presented here.

HydroSTAR performs simulations in the frequency domain. Thus, the conversion must be applied to enable comparison of the results with those of SHIP_Motion. The equation used for conversion is as follows:

$$\lambda = \frac{2\pi}{\omega^2} \times g \tag{13}$$

where λ is the wavelength, ω is the frequency, and g is the gravitational acceleration.

The equation used to convert the added resistance into the added resistance coefficient C_{aw} is:

$$C_{aw} = \frac{R_{aw}}{\rho g A^2 B^2 / L_{pp}} \tag{14}$$

where R_{aw} is the predicted added resistance, ρ is the water density, A is the wave amplitude, B is the ship's breadth, and L_{pp} is the length between perpendiculars.

The simulation results of added resistance prediction using PF solver, together with a comparison with RaNS simulation results, are shown in Fig. 6. Since the results only show the first-order resistance prediction, the accuracy of the prediction is quite limited. The PF results also show unexpected drops in resistance at certain wavelengths, which is generally not observed in the RaNS simulations and EFD data. This finding may be explained by the presence of irregular frequencies in the simulation and the linear assumptions used in PF solvers. However, if the third-order polynomial line of the HydroSTAR results is considered, the agreement between the two solvers is quite reasonable up to 0.7 L_{pp}. In general, PF solvers are more promising in generating the overall added resistance curve than other solvers; however, the former fails to predict the resistance with adequate accuracy in short-wavelength regions (Sadat-Hosseini et al. 2013) mainly because, in short-wavelength cases, the ship's interaction with the incident waves is of primary importance, which creates a mostly non-linear response. Thus, the linear assumption in PF solvers limits their accuracy in short-wavelength regions. However, the anomaly of the results obtained at relatively large wavelengths may be attributed to ignorance of second-order wave structure interactions.

In general, PF-based solvers are considered more reliable in predicting motion rather than added resistance in short waves. The heave and pitch RAO prediction results obtained by HydroSTAR, together with the RaNS simulation results, are shown in Fig. 7.

The RAO results basically agree well with each other. The heave RAO results of the PF and RaNS solvers agree very well with each other for most of the presented wavelengths, except near the resonance area. The pitch RAO results calculated by both solvers show a very similar trend with slight deviations in values. The observed discrepancies may be attributed to the different KG values used by the RaNS and PF solvers. Overall, the results

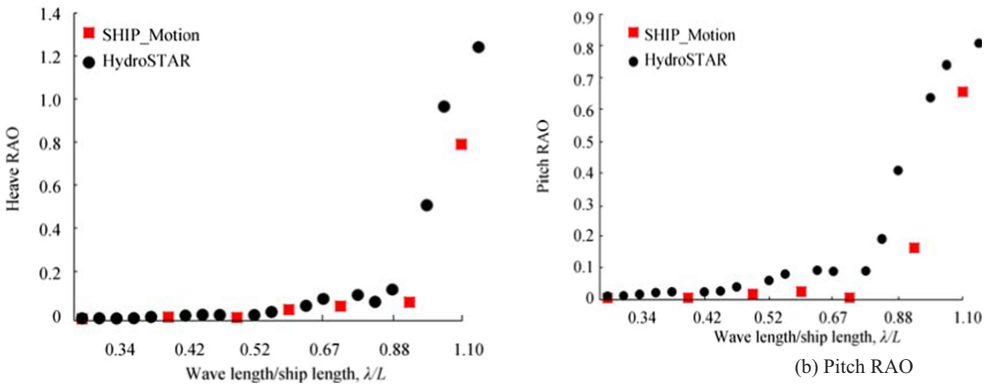

(a) Heave RAO

(b) Pitch RAO

Fig. 7 Heave and pitch RAO predicted for the JBC using SHIP_Motion and HydroSTAR

from both the methods agree well enough to establish reliability of the simulated results.

4 Conclusion

This paper presents simulation results for the JBC model in both calm water and head waves. First, RaNS simulation was performed for calm water, and the results were compared with the experimental data. Next, simulations were performed for a range of Froude numbers. Finally, head wave simulation results were generated using the RaNS and PF solvers for short waves.

The calm water RaNS simulation, which was run with a mesh resolution of 1.1 million, shows a deviation of only 1.16% in comparison with the experimental data for total resistance prediction. The sinkage shows a deviation of 8.14%. However, the actual deviation is limited to only a few millimeters. The trim results show a deviation of 33%, likely because of the difference in KG values between the experimental and simulation settings.

The head wave simulations, which were run using the RaNS- and PF-based solvers, were used to predict C_{aw} and heave and pitch RAOs. Considering the previous validation results for added resistance prediction using the RaNS solver with similar hull forms, the results of C_{aw} for the JBC may be considered to be accurate within 10%. According to Shigunov et al. (2018), a deviation of 15% in resistance prediction can affect the propulsion prediction by 5%. Thus, a 10% uncertainty is within the acceptable range. Furthermore, the agreement in results between the two solvers (within the regular operational range) ensures that the presented results have sufficient reliability.

Overall, the presented results may be concluded to be reliable enough to be considered initial reference data for further studies using the JBC model. This study also reveals that the concepts of CFD in ship hydrodynamics have reached sufficient maturity to produce reliable insights into the general characteristics of a hull form in an economical and efficient manner.

References

Akimoto H, Miyata H (2002) Finite-volume simulation method to predict the performance of sailing boat. J Mar Sci Technol 7:31–42. https://doi.org/10.1007/s007730200011

Celik IB, Ghia U, Roache PJ, Freitas CJ, Coleman H, Raad PE (2008) Procedure for estimation and reporting of uncertainty due to discretization in CFD applications. J Fluids EngTrans ASME 2008:078001. https://doi.org/10.1115/1.2960953

Chen X-B (2004) Hydrodynamics in offshore and naval applications - part I. Perth, Australia, November, 2004

Chen X-B, Rezende F (2009) Efficient computations of second-order low-frequency wave load. 28th International Conference on Ocean, Offshore and Arctic Engineering, Honolulu, 2009. OMAE2009–79522, 525–532. https://doi.org/10.1115/OMAE2009-79522

Deng GB, Queutey P, Visonneau M (2010) RANS prediction of the KVLCC2 tanker in head waves. J Hydrodyn 22(5):476–481. https://doi.org/10.1016/S1001-6058(09)60239-0

Faltinsen OM, Minsaas KJ, Liapis N, Skjørdal SO (1980) Prediction of resistance and propulsion of a ship in a seaway. In Proceedings of 13th Symposium on Naval Hydrodynamics, Monterey CA

Fuji H, Takahashi T (1975) Experimental study on the resistance increase of a ship in regular oblique waves. Proceedings of the 14th ITTC 4, Ottawa: 351–360

Gerritsma J, Beukelman W (1972) Analysis of the resistance in waves of a fast cargo ship. International Shipbuilding Progress 19(217):285–293. https://doi.org/10.3233/ISP-1972-1921701

Islam H, Akimoto H (2015) Prediction of ship resistance in head waves using RaNS based solver. International Conference on Mechanical Engineering (ICME), BUET, Dhaka, 2015. https://doi.org/10.1063/1.4958371

Islam H, Rahman MM, Islam MR, Akimoto H, Afroz L (2017) Comparative study of RaNS and PF based solver for predicting added resistance of a very large crude carrier. Procedia Eng 194:74–81. https://doi.org/10.1016/j.proeng.2017.08.119

Islam H (2015) Prediction of ship resistance in oblique waves using RaNS based solver. MS Thesis, Division of Ocean Systems Engineering, KAIST, 2015

Journee JMJ (2001) Verification and validation of ship motion program SEAWAY. Report 1213a, Shiphydrodynamics laboratory, Delft University of Technology, 2001

Kashiwagi M (2009) Impact of hull design on added resistance in waves—application of the enhanced unified theory. Proceedings of the 10th International Marine Design Conference, Trondheim, Norway. 2009. pp 521–535

Kim K-H, Kim Y (2011) Numerical study on added resistance of ships by using time-domain Rankine panel method. Ocean Eng 38:1357–1367. https://doi.org/10.1016/j.oceaneng.2011.04.008

Kim J, Park I-R, Kim K-S, Kim Y-C, Kim YS, Van S-H (2013) Numerical towing tank application to the prediction of added resistance performance of KVLCC2 in regular waves. Proceedings of the Twenty-third (2013) International Offshore and Polar Engineering (ISOPE). Anchorage, Alaska, USA, June 30–July 5, 2013. ISOPE-I-13-348

Kim H, Akimoto H, ISlam H (2015) Estimation of the hydrodynamic derivatives by RaNS simulation. Ocean Eng 108:129–139. https://doi.org/10.1016/j.oceaneng.2015.08.010

Kim M, Hizir O, Turan O, Incecik A (2017) Numerical studies on added resistance and motions of KVLCC2 in head seas for various ship speeds. Ocean Eng 140:466–476, 2015. https://doi.org/10.1016/j.oceaneng.2017.06.019

Larsson L, Stern F, Bertram V (2003) Benchmarking of computational fluid dynamics for ship flows: the Gothenburg 2000 workshop. J Ship Res 47:63–81 2003

Larsson L, Stern F, Visonneau M (2011) CFD in ship hydrodynamics-results of the Gothenburg 2010 workshop. Marine 2011, IV International Conference on Computational Methods in Marine Engineering, Computational Methods in Applied Sciences, 2011. https://doi.org/10.1007/978-94-007-6143-8_14

Maruo H (1957) The excess resistance of a ship in rough sea. Int Shipbuild Prog 4:337–345

Moctar B, Kaufmann J, Ley J, Oberhagemann J, Shigunov V, Zorn T (2010) Prediction of ship resistance and ship motions using RANSE. In: Proceedings of Gothenburg 2010: A Workshop on CFD in Ship Hydrodynamics

Ock YB (2014) Numerical simulations of added resistance around ships in regular head waves using overset grids. MS Thesis, Department

of Naval Architecture and Ocean Engineering, Pusan National University, 2014 (in Korean)

Orihara H (2005) Development and application of CFD simulation technology for the performance estimation of ship in waves. PhD Thesis, Tokyo University, 2005 (in Japanese)

Orihara H, Miyata H (2003) Evaluation of added resistance in regular incident waves by computational fluid dynamics motion simulation using an overlapping grid system. J Mar Sci Technol 8:47–60. https://doi.org/10.1007/s00773-003-0163-5

Pelaez JG, Papanikolaou A, Gonzalez V (2000) Numerical and experimental study on the seakeeping performance of a fast round-bilge mono hull. Proceedings of the 4th Osaka Colloquium on Seakeeping Performance of Ships. Cosmosquare Int. Education and Training Center, Osaka, Japan

Sadat-Hosseini H, Wu P-C, Carrica PM, Kim H, Toda Y, Stern F (2013) CFD verification and validation of added resistance and motions of KVLCC2 with fixed and free surge in short and long head waves. Ocean Eng 59(2013):240–273. https://doi.org/10.1016/j.oceaneng.2012.12.016

Sadat-Hosseini H, Carrica P, Kim H, Toda Y, Stern F (2010) URANS simulation and valiation of added resistance and motions of the KVLCC2 crude carrier with fixed and free surge conditions. In: Proceedings of Gothenburg 2010: A Workshop on CFD in Ship Hydrodynamics

Seo M-G, Yang K-K, Park D-M, Kim Y (2014) Numerical analysis of added resistance of ships in short waves. Ocean Eng 87:97–110. https://doi.org/10.1016/j.oceaneng.2014.05.011

Shen Z, Wan D, Carrica PM (2015) Dynamic overset grids in OpenFOAM with application to KCS self-propulsion and maneuvering. Ocean Eng 108:287–306. https://doi.org/10.1016/j.oceaneng.2015.07.035

Shigunov V, el-Moctar O, Papanikolaou A, Potthoff R, Liu S (2018) International benchmark study on numerical simulation methods for prediction of manoeuverability of ships in waves. Ocean Eng 165:365–385. https://doi.org/10.1016/j.oceaneng.2018.07.031

Sigmund S, el Moctar O (2018) Numerical and experimental investigation of added resistance of different ship types in short and long waves. Ocean Eng 147(2018):51–67. https://doi.org/10.1016/j.oceaneng.2017.10.010

Simonsen CD, Otzen JF, Joncquez S, Stern F (2013) EFD and CFD for KCS heaving and pitching in regular head waves. J Mar Sci Technol 18:435–459. https://doi.org/10.1007/s00773-013-0219-0

Söding H, Shigunov V, Schellin TE, Moctar O (2014) A Rankine panel method for added resistance of ships in waves. ASME J Offshore Mech Arct Eng 136(3):031601-031601-7. https://doi.org/10.1115/1.4026847

Tokyo 2015 Workshop, JBC, 2015. [Online]. Available: http://www.t2015.nmri.go.jp/jbc_gc.html. Accessed 2016